PHYSICAL REVIEW B VOLUME 28, NUMBER 2 15 JULY 1983

Quenched ω phase in a Ti-V alloy

C. B. Walker
U.S. Army Materials and Mechanics Research Center, Watertown, Massachusetts 02172
(Received 29 November 1982)

A study has been made of the ω phase in a quenched Ti—23 at. % V alloy at room temperature using single-crystal x-ray-diffraction techniques. The ω phase appears as coherent particles with an average volume of ~ 2500 unit cells. An observed slow time dependence of the diffraction patterns shows that the ω-phase transformation continues to progress at room temperature until finally, 16 months after the quench, the alloy has almost completely transformed. The various ω-phase peaks display significant differences in width, and so both peak widths and peak intensities are used as data to be matched by structural models. The five acceptable models found have three common characteristics: (1) The ω-phase displacements are position dependent, *not* uniform, varying steeply from a large value at the particle center to zero at the boundary; (2) the displaced atoms have very anisotropic, anharmonic "temperature factors"; and (3) the particle is shaped as a thick, rectangular platelet, with its plane parallel to $\{112\}$ and its long dimension along [111], supporting a Hatt-Roberts model of the transformation. We suggest that position-dependent displacement distributions and anisotropic, anharmonic temperature factors should be a characteristic of all quenched, imperfect ω phases.

I. INTRODUCTION

The athermal ω phase is a metastable phase found in alloys of Zr or Ti with various group-V*B* and -VI*B* elements on quenching from the high-temperature β- (bcc-) phase solid-solution region.[1,2] The basic structural studies were made by Silcock and co-workers[3,4] and Bagariatskii and co-workers.[5,6] The crystallography has been summarized by Keating and LaPlaca.[7] The transformation from β to ω phase involves ordered displacements along a [111] direction that shift two adjacent (111) planes of atoms towards one another, while the third (111) plane in the normal β-phase stacking sequence stays fixed. In a "perfect" ω phase, atomic displacements of $\pm a\sqrt{3}/12$ (~ 0.5 Å) bring the two planes completely together into a single central plane, giving the hexagonal $\mathrm{AlB_2}$ structure, but in real quenched alloys this structure is thought to be reached only in alloys of low solute content, with alloys of higher content showing progressively smaller average displacements and only trigonal symmetry.[8–11] The size of a quenched ω-phase particle also decreases with increasing solute content, causing much weaker and more diffuse diffraction patterns.[11–13]

Recent neutron studies[14,15] of Zr-Nb ω-phase-forming alloys have found the short-wavelength phonon groups to be poorly defined, indicating strong anharmonicity, and have shown the existence of strong, quasistatic ω-phase-like short-range structural fluctuations at high temperatures well into the β-phase solid-solution field. Other studies[11,16] have suggested that the metastable ω-phase particles at and below room temperature in these alloys are actually dynamic ω-phase-like structural fluctuations whose size and time dependence vary strongly with composition, ranging from quite large and long-lived ω-phase regions at low solute content to small regions with a wide spectrum of characteristic times at high solute content, and with a statistically constant volume fraction of ω-phase-like regions at any one temperature that changes reversibly with temperature.

Information on the structure of quenched, imperfect ω phases is sparse and of uncertain value. Analyses of diffracted intensities, sometimes from as few as two reflections, generally have been based on a simple uniform structure factor model, regardless of particle size, with more complex models used in only two instances,[17,18] and every study seems to have assumed a common isotropic, harmonic temperature factor for all atoms.

The principal objective of the present x-ray study is to obtain a detailed description of the structure of a quenched, imperfect ω phase in a Ti-V alloy. Ti and V atoms have almost equal x-ray scattering factors, and so the ω-phase scattering is due almost completely to the atomic displacements, with only weak extraneous scattering from possible atomic ordering. The x-ray measurements are all made at room temperature, so a separation of the scattering into static versus dynamic or elastic versus inelastic components is not possible.

The recent electron diffraction study of quenched Ti-V alloys by McCabe and Sass[13] shows the general variation of ω-phase scattering as a function of composition[19]—at 13 at. % V there are sharp crystalline peaks; for 15, 19, and 25 at. % V the peaks broaden, weaken, and shift parallel to [111], but remain reasonably crystalline in appearance, and there is increasing diffuse scattering; and for compositions ≥ 35 at. % V the scattering peaks are weaker, broader, and more diffuse, not really crystalline in appearance, and with still greater [111] shifts. Other x-ray and electron studies of quenched Ti-V alloys give a somewhat different result, reporting that a 19 at. % V alloy either shows no ω phase[20,21] or is nearly the upper limit for ω-phase formation.[22] In further contrast, other electron-diffraction studies[23,24] on a 19 at. % V alloy report the occurrence of an apparently reversible ω-phase transformation on cooling through an "omega start" temperature of approximately $-20\,^{\circ}\mathrm{C}$. Such conflicting results may result from differences in the samples (quench rates, O_2 content,[24] composition errors) and in the experimental procedures and resolution, plus the subjectivity of particle-nonparticle pattern interpretations.

II. EXPERIMENTAL DETAILS

A Ti-V alloy single crystal, approximately $11\times13\times2$ mm^3, was provided by S. L. Sass of Cornell University. The crystal had been annealed 5 h at $1000\,^{\circ}\mathrm{C}$ ($\sim 350\,^{\circ}\mathrm{C}$ up into the β-phase region) in a vacuum of 8×10^{-6} Torr, quenched into diffusion pump oil at room temperature, and given a light chemical etch. Subsequent analysis[25] of a part of the crystal gave the composition as 22.6 ± 1.0 at. % V, with an O_2 content of 160 wt. ppm, and with other impurities (W, Fe, etc.) totaling $\sim$0.01 at. %. X-ray fluorescence tests over the crystal face indicated that composition variations were limited to $\pm1\%$ of the average composition.

The primary beam was Cu$K\alpha$ radiation from a Picker constant potential x-ray generator operated at 30 kV and 16 mA, monochromated by diffraction from a 0.009-in.-thick LiF crystal that had been plastically bent against a toroidal form and mounted on an open-backed holder, with the beam focused to a small rectangular cross section at the diffractometer axis (90% of beam power within a 0.019 in. width and a 0.058 in. height). The primary beam horizontal divergence was 0.68° full width at half maximum (FWHM), the receiver slit width was 1.05°, and the combined slit—primary-beam vertical divergence was 1.32° FWHM, which corresponds to linear traces of the diffraction vector in reciprocal space of 0.0249, 0.0384, and 0.0485, respectively (in units of a_0^{-1}). The measured beam polarization ratio was 0.707 ($\pm1\%$). The scattering radiation was detected with a NaI(Tl) scintillation detector and a single-channel pulse-height analyzer. A 0.003 in. Al foil before the receiver slit strongly attenuated the Ti and V fluorescence, reducing the average background to <2 counts/sec. The half-wavelength radiation passed by the monochromator and detector-analyzer was 1:45 000 compared to the Cu$K\alpha$ radiation, as seen from its very weak low-angle β-phase reflections, which would give negligible effects at the ω-phase peaks; and no higher-order contamination could be detected. The Picker x-ray generator was advertised as ultrastable, with a kV stability of 0.1% and a mA stability of 0.02%. To check for long-term beam changes due to possible tube and/or monochromator aging, measurements of the (222) reflection were repeated at various times, but it was found (see Sec. III) that changes were occurring in the alloy itself throughout the 15 months of measurements at room temperature, and no accurate long-term beam stability check was achieved.

The alloy crystal was attached with beeswax to a holder on a G.E. quarter-circle goniometer mounted on a Picker diffractometer, and was oriented so the [111] direction was parallel to the ϕ axis. The crystal face was found to be at an angle of 1.9° to the (111) plane, causing miscut absorption effects that generally were eliminated[26] by averaging intensities using the threefold symmetry of the [111] axis. The four diffractometer axes were driven by Slo-Syn stepping motors controlled by a Digital Equipment Corp. PDP-8 computer. The computer unit also included a completely interfaced 12-bit binary scalar for counting the x rays, an internal clock, various pulses, relays, and voltages to control devices, and an input register for external contact closure and voltage level signals. This computer unit, with associated subroutine packages, allowed complete automation of a variety of lengthy diffraction experiments, including preliminary angle calculations, antibacklash angle setting, and intensity measurement and minor data processing, with output on an ASR-33 teletype. All measurements were made at room temperature in air, with the air scattering held to <1 count/sec except at low angles by auxiliary slits along both primary and scattered beam paths.

III. EXPERIMENTAL OBSERVATIONS

A. General

X-ray scattered intensities were measured at rectangular grids of points in the bcc $(1\bar{1}0)$ plane through every β- and ω-phase reciprocal-lattice point (RLP) within the accessible region, $2\theta<161^{\circ}$. The results are shown in Fig. 1, where we plot contours of constant intensity for the raw experimental data, uncorrected even for background. The background is $\simeq$2 counts/sec except at the lowest angles; the successive dotted contours show intensities of 5, 10, 15, and 20 counts/sec; the solid contour marks one-half the intensity of the peak above background; and the adjoining number gives the peak intensity in counts/sec. The β-phase RLP's are indicated by dots.

To help understand Fig. 1, we sketch in Fig. 2 the superposed arrays of β- and ω-phase RLP's found in this $(1\bar{1}0)$ plane. The ω phase can form with its $\vec{c}$ axis parallel to any one of the four $\{111\}$ directions in the parent β phase, these usually being referred to as the four ω variants, but only two of these variants ($\omega_{\mathrm{I}}{:}\vec{c}\,||[111]$, and $\omega_{\mathrm{II}}{:}\vec{c}\,||[11\bar{1}]$) have RLP's in this plane not coincident with β-phase RLP's. The ω_{I} RLP's, indexed here as $(h\,0{\cdot}l)$, fall in layer lines (constant l) perpendicular to [111], and the ω_{II} RLP's, indexed as $(0k{\cdot}l)$, fall in layer lines perpendicular to $[11\bar{1}]$. All four ω-phase variants have RLP's coincident with the β-phase RLP's. There can be appreciable intensity differences between the various ω-phase reflections, depending on the atomic displacements.

The scattering distribution from our Ti-V ω phase plotted in Fig. 1 is seen to be primarily small particlelike rather than diffuse in character, in that the intensity is concentrated mainly in broadened peaks around the RLP's of the two ω-phase variants, with FWHM's approximately twice the FWHM of the β-phase reflections, and there is only weak diffuse scattering joining some adjacent ω-phase peaks. The overall appearance of the broadened peaks yields a first crude description of an average ω-phase particle in the alloy as being rodlike, with its long axis parallel to $\vec{c}$ and a length-to-diameter ratio of $\sim$2, and the peak sharpness indicates a particle length of more than 20 unit cells. Despite this rather large particle size, the marked inequality of the peak intensities of the $l=3$ symmetric pairs [e.g., $(10{\cdot}3)$ and $(\bar{1}0{\cdot}3)$] shows that the average atomic displacements are significantly smaller than those for a "perfect" hexagonal ω phase. The peaks show other features, not easily visible in the figure, that should be noted: (1) There are significant differences between

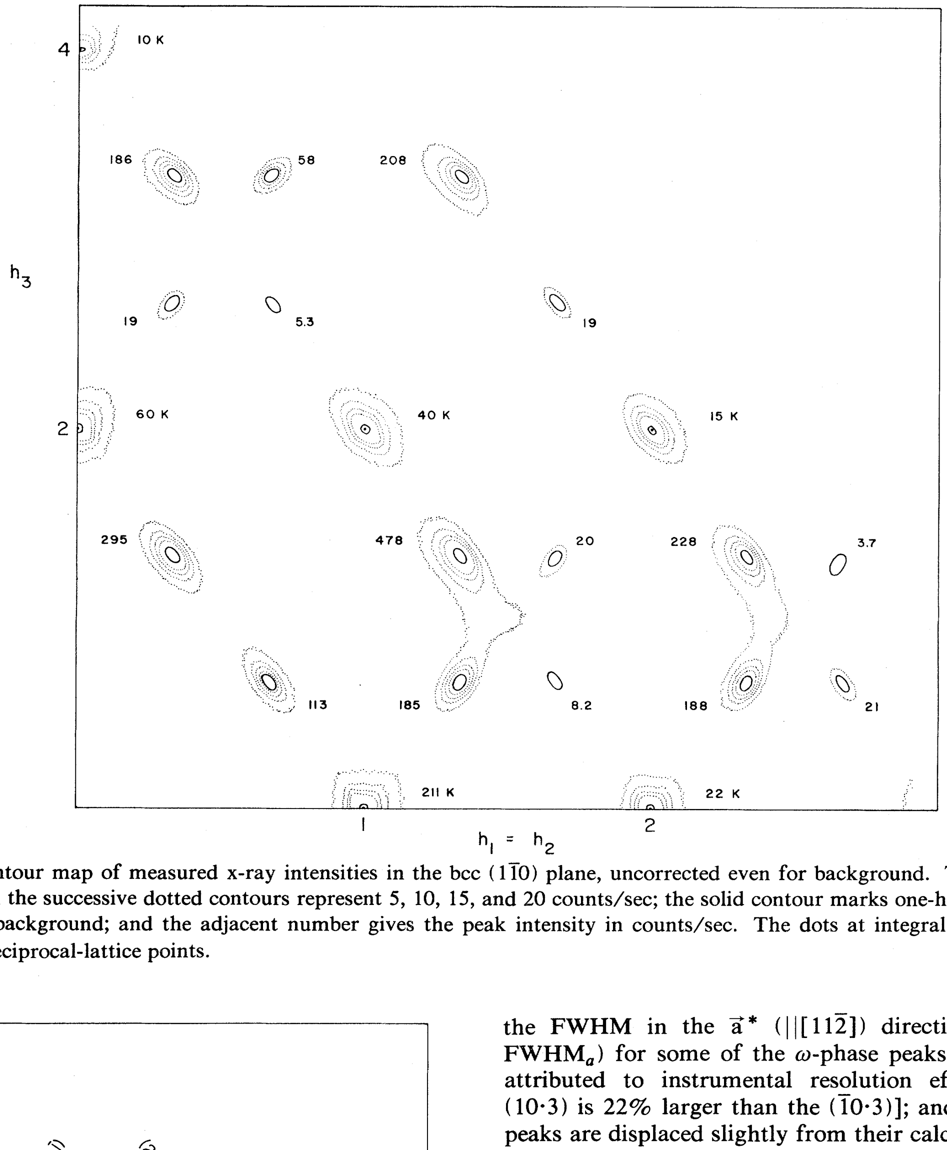

FIG. 1. Contour map of measured x-ray intensities in the bcc $(1\bar{1}0)$ plane, uncorrected even for background. The background is $\simeq 2$ counts/sec; the successive dotted contours represent 5, 10, 15, and 20 counts/sec; the solid contour marks one-half the intensity of a peak above background; and the adjacent number gives the peak intensity in counts/sec. The dots at integral coordinate values mark the bcc reciprocal-lattice points.

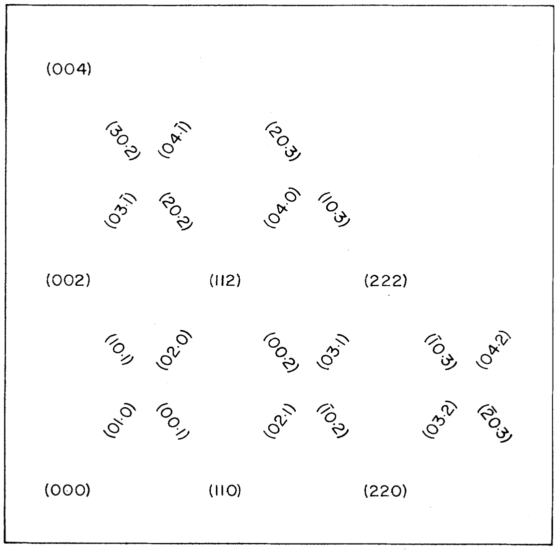

FIG. 2. Sketch locating and identifying various β- and ω-phase reciprocal-lattice points in the bcc $(1\bar{1}0)$ plane. The $(0k\cdot0)$ ω-phase reflections, with $k \neq 3n$, are generally expected to have negligible intensities.

the FWHM in the $\vec{a}^*$ $(\|[11\bar{2}])$ direction (henceforth, FWHM_a) for some of the ω-phase peaks that cannot be attributed to instrumental resolution effects [e.g., the $(10\cdot3)$ is 22% larger than the $(\bar{1}0\cdot3)$]; and (2) the diffuse peaks are displaced slightly from their calculated RLP positions, with the displacement generally directed along $\vec{c}$ away from the nearest β-phase RLP, and with a few reflections also showing $\vec{a}^*$ displacement components.

The diffuse bridges connecting adjacent peaks show interesting differences in shape and intensity. The two bridges in Fig. 1, joining $(00\cdot2)$ to $(02\cdot1)$ and $(\bar{1}0\cdot3)$ to $(03\cdot2)$, both show an anomalous width near the center, with maximum intensities above background on the bisecting line, $h_3 = 1$, of 6 and 4 counts/sec, respectively, and measurements in a vertical plane containing this line through the $(00\cdot2)$-$(02\cdot1)$ bridge show the intensities decrease with increasing height above the $(1\bar{1}0)$ plane, giving the bridge a tapered rod cross section. Conversely, there is no evidence of any such bridge, to within 0.5 counts/sec above background, between the adjacent, reasonably intense $(30\cdot2)$ and $(04\cdot\bar{1})$ peaks. The bridge between the $(10\cdot1)$ and $(00\cdot1)$ peaks, both of the same ω-phase variant, has a different shape, as is shown in Fig. 3. The constant intensity contours here suggest a repulsion between the scattering from the two peaks. This figure also shows the

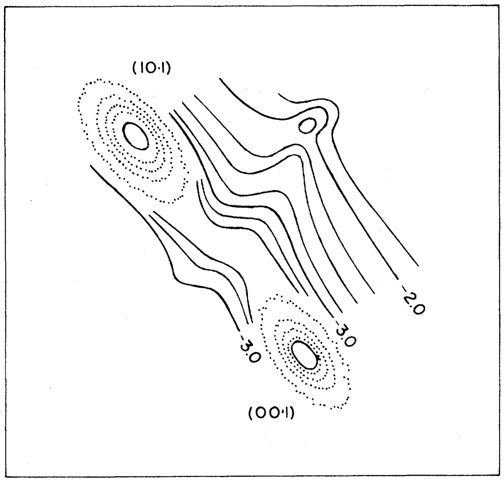

FIG. 3. Contour map at a finer scale of the measured, uncorrected intensity distribution in a section of the bcc $(1\bar{1}0)$ plane containing the (00·1) and (10·1) ω-phase peaks. The successive solid contours represent 1.9, 2.0, 2.2, 2.4, 2.7, 3.0, 3.3, and 3.6 counts/sec; the dotted contours are as in Fig. 1. The intensity at the bridge saddle point is 3.8 counts/sec. The very weak peak near the (02·0) RLP has an intensity of 2.3 counts/sec.

presence of a very weak peak ($\sim$0.3 counts/sec above background) displaced somewhat in the [112] direction from the (02·0) RLP, plus a possible weaker, second peak superposed on the ridge from the (00·1) on the opposite side of the (02·0) RLP. Similar very weak, unequal split peaks are also seen around the (04·0) RLP. The $(0k\cdot0)$ reflections, with $k \neq 3n$, are forbidden ω-phase reflections, whose intensity is generally expected to be zero for any magnitude of ω-phase displacement.

Our primary finding of broadened, crystalline ω-phase peaks suggesting small rodlike particles, with intensity differences demonstrating trigonal symmetry, seems in general agreement with the results of McCabe and Sass,[13] and disagrees with the other studies reporting no ω phase at this composition.[20–24] The diffuse bridges are somewhat similar to the bridges seen in McCabe's patterns, where multiple scattering effects would obscure intensity and shape differences. However, McCabe observed ω-phase peak displacements parallel to $\vec{c}$, directed away from the nearest β-phase RLP, that were approximately ten times greater for this composition than those observed here. McCabe also concluded that no real $(0k\cdot0)$ reflections were present, and she reported the existence of $\{111\}$ planes of diffuse intensity that are not observed in our measurements.

Finally, one should note the difference in shape of the scattering contours around the various β-phase RLP's, as, for example, the (222) and (220). All four ω variants have RLP's coincident with each β-phase RLP, and the differences in contour shapes are thought to reflect differences in the relative intensity of the corresponding reflections for the different variants. No such differences have been observed in previous contour maps of quenched ω-phase alloys.[11,14]

B. Time dependence

The measurements plotted in Fig. 1 were taken mainly during a three-week period beginning six weeks after the sample anneal and quench. Two months later repeats of some of the measurements showed discrepancies exceeding the estimated errors. Further repeats of various measurements during the ensuing twelve months established the following trends.

(a) The peak intensities of the ω-phase reflections generally increased with time after the quench. Figure 4(a) shows the observed variation of the (00·2) peak intensity. Most of the other peaks behaved similarly, but the weak $(\bar{1}0\cdot2)$ and (20·2) peaks appeared constant to within $\pm 3\%$. The few data on ω-phase peak FWHM, both in the $\vec{c}^{\,*}$ and $\vec{a}^{\,*}$ directions, indicated these remained constant within $\pm 2\%$.

(b) The intensities of the diffuse bridges between ω-phase reflections decreased with time. This is illustrated in Fig. 4(b), where we plot the variation of the maximum intensity above background on the bisecting line through the (00·2)-(02·1) bridge.

(c) Double integrals of the β-phase reflection intensities, $E = \int\int (I - B) d\Omega\, d\theta$, taken with the normal diffractometer slits, varied from a monotonic, 14% decrease for the (400) to an initial 4% increase (17 weeks) followed by a slow 1% decline for the (110). The data for the (222) are shown in Fig. 4(c).

(d) The bcc lattice parameter a_0 determined from a $\cos^2\theta$ extrapolation of the centers of gravity of the (400),

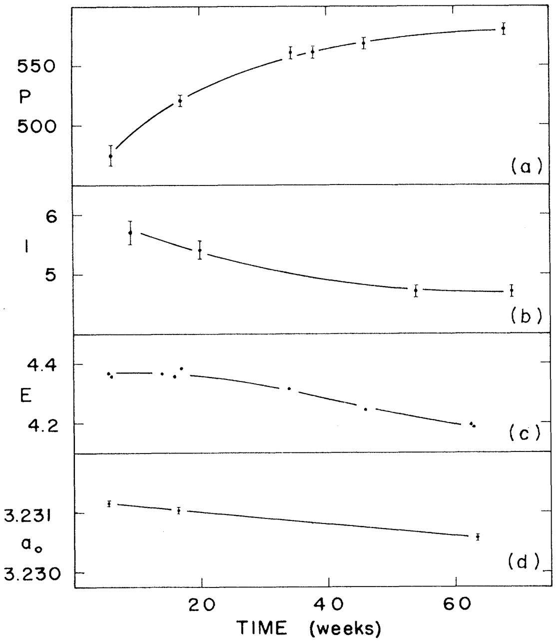

FIG. 4. Observed time dependence of various quantites: (a) the peak intensity of the (00·2) reflection, in counts/sec; (b) the maximum intensity above background along the line, $h_3 = 1$, through the (00·2)-(02·1) bridge, in counts/sec; (c) an integral of the intensity in the (222) reflection, in 10^6 counts; and (d) the bcc lattice parameter, in Å units.

(321), and (222) reflections, decreased almost linearly with time, as is shown in Fig. 4(d).

The ω-phase transformation in this alloy clearly has continued to develop to a significant extent while at room temperature, a feature that has not been reported in any other ω-phase transformation study. The exponential slowing of the growth of the ω-phase peak intensities, with a time constant of $\sim$20 weeks, suggests that the ω phase is close to metastable equilibrium by the end of our measurements.

C. Intensities and FWHM of ω peaks

The intensities of the ω peaks were measured at five times after the initial general contour mapping, as shown in Fig. 4(a). The final measurements, made 16 months after the quench, consisted of a short scan along the $\vec{c}^{\,*}$ direction through the peak maximum plus background measurements on each side, all repeated with ϕ incremented in steps of 120° to use the threefold symmetry of the [111] axis, together with a pair of complete peak profiles by scans through the peak parallel to $\vec{c}^{\,*}$ and to $\vec{a}^{\,*}$, for each of the 16 ω peaks in the accessible region of the $(1\bar{1}0)$ plane. Individual values of the maximum intensity I_τ for an ω-phase peak were obtained from each of its threefold related short scans and its two profiles by fitting parabolas to those intensities $\geq 0.93 I_\tau$. The set of I_τ values for the threefold related scans for the eight stronger peaks were used to evaluate the parameters defining the sample surface miscut. Then, for each peak, an average of the I_τ values from the profile scans, corrected for surface miscut, was combined with an average of the I_τ values from the threefold related scans, which is independent of miscut, to yield the average observed intensity for that peak. The standard deviation associated with that intensity was taken to be the count statistics error of a single measurement, a balance of the error reduction obtained by averaging and the actual larger-than-expected scatter shown in the miscut absorption analysis. The background correction to the peak profiles generally was obtained by linear interpolation, but for the weaker peaks adjacent to diffuse bridges a more curved background trace was interpolated to match smoothly with the bridge. The uncertainty in this background interpolation proved large for the very weak (04·2) peak, so this peak was dropped from further consideration.

The average observed intensity and peak profiles for the remaining 15 ω-phase peaks were corrected for atomic scattering factors,[27] polarization factors, and instrumental broadening. The broadening correction was derived from the formulation of Walker and Chipman,[28] neglecting wavelength spread and assuming that the true intensity distribution around the RLP, $\vec{\tau}$, could be written as

$$J(\vec{\tau}+\vec{v})=J_0(\vec{\tau})C(v_c)A(v_t)\ ,$$

where v_c and v_t are the components of $\vec{v}$ parallel and perpendicular, respectively, to $\vec{c}^{\,*}$, and $C(0)=A(0)=1$. The scattered power measured at $\vec{\tau}+\vec{d}$, expressed in the same units as $J_0(\vec{\tau})$, can then be obtained as

$$P(\vec{\tau}+\vec{d})=J_0(\vec{\tau})\int\int\int f_1(p_1)f_2(p_2)f_3(p_3)C(d_c+p_c)A(d_t+p_t)dp_1dp_2dp_3\ , \qquad (1)$$

where $p_i=(a_0/\lambda)\alpha_i$, a dimensionless variable involving the divergence angle, α_i; and f_1, f_2, and f_3 are measured distribution functions characterizing the primary beam horizontal divergence, the receiver slit width, and the combined vertical divergence, respectively, each normalized so that $\int f_i(p_i)dp_i=1$. Then, after adjusting assumed functions $C(x)$ and $A(y)$ until the calculated FWHM$_c$ (the FWHM in the $\vec{c}^{\,*}$ direction) and FWHM$_a$ for a given $\vec{\tau}$ matched the observed FWHM values for that peak, the multiplicative instrumental broadening correction to the peak intensity is given by

$$R(\vec{\tau})=J_0(\vec{\tau})/P(\vec{\tau})$$

and the corrected FWHM$_c$ and FWHM$_a$ are just the FWHM of the functions $C(x)$ and $A(y)$, respectively. The observed intensities are in arbitrary units, so only the relative values of $R(\vec{\tau})$ for the different reflections are significant. For our calculations the unbroadened functions $C(x)$ and $A(y)$ for a peak were assumed to be given by its observed peak profiles in the $\vec{c}^{\,*}$ and $\vec{a}^{\,*}$ directions, respectively, each with its step size scaled down by an adjustable parameter. This correction for the different peaks gave a reduction in FWHM$_c$ ranging from 11% to 34%, a reduction in FWHM$_a$ ranging from 5% to 18%, and a normalized peak intensity multiplier varying from 1.083 to 0.855. An alternate calculation assumed $C(x)$ and $A(y)$ to be Gaussian to obtain an estimate of the uncertainty in the correction due to the choice of unbroadened shape, and two other calculations estimated the uncertainties due to errors in the observed FWHM and to errors in the measured, larger vertical divergence distribution function.

The final corrected data for these 15 ω-phase peaks are shown in Table I. The peaks are grouped in "families" [e.g., the (00·2), (30·2), and (03·2)], whose members all have the same geometrical structure factor in the absence of temperature factors. The peak intensities, in arbitrary units, range through 2 orders of magnitude. The estimated standard deviation for a peak intensity, obtained by combining the errors due to count statistics, the uncertainty in the beam polarization ratio, and the various uncertainties in the broadening correction, varies from 1.4% for the strong (00·2) to 4.1% for the weak (20·2). The FWHM$_c$ are essentially the same for most peaks, with only the (10·3) family showing different, larger values, but the FWHM$_a$ values, while reasonably consistent within a family, show an appreciable spread among the different families. To estimate the precision of these FWHM, we treat the scatter of values within a family as statistical fluctuations and average the values of σ^2 so obtained from each of the 3 three-member families. That estimate for the standard deviation of a single FWHM$_c$ is $0.0010\,|\vec{c}^{\,*}|$, and the estimated standard deviation of a single FWHM$_a$ is $0.0027\,|\vec{a}^{\,*}|$, both approximately 3% errors. An average of the FWHM for the strong (00·2) family gives FWHM$_c=0.0338\pm0.0006$ (units of $|\vec{c}^{\,*}|$)

TABLE I. Final ω-phase peak intensity and FWHM data. Intensities are in arbitrary units; FWHM_c and FWHM_a in units of $|\vec{c}^*|$ and $|\vec{a}^*|$, respectively.

	Intensity	FWHM_c	FWHM_a	NFWHM_c	NFWHM_a
(00·2)	3.3739±0.0475	0.0342	0.0861	1.000	1.000
(30·2)	2.5261±0.0373	0.0323	0.0888		
(03·2)	2.4343±0.0360	0.0350	0.0891		
(10·1)	1.0536±0.0237	0.0342	0.0975	1.011±0.025	1.081±0.027
(02·1)	1.0032±0.0234	0.0351	0.0936		
(04·$\bar{1}$)	0.7593±0.0178	0.0332	0.0942		
($\bar{1}$0·3)	2.7490±0.0418	0.0338	0.0846	0.994±0.027	0.951±0.028
(20·3)	2.4814±0.0386	0.0335	0.0828		
(00·1)	0.2667±0.0064	0.0338	0.0990	0.991±0.024	1.175±0.028
(03·1)	0.1772±0.0046	0.0330	0.1047		
(03·$\bar{1}$)	0.1696±0.0045	0.0338	0.1065		
(10·3)	0.1987±0.0052	0.0371	0.1101	1.083±0.028	1.262±0.032
($\bar{2}$0·3)	0.1944±0.0051	0.0362	0.1119		
($\bar{1}$0·2)	0.0406±0.0014	0.0338	0.1074	1.014±0.028	1.215±0.031
(20·2)	0.0295±0.0012	0.0348	0.1065		
	{00·2}:	$\overline{\mathrm{FWHM}}_c=0.0338\pm0.0006$,	$\overline{\mathrm{FWHM}}_a=0.0880\pm0.0016$		

and $\mathrm{FWHM}_a=0.0880\pm0.0016$ (units of $|\vec{a}^*|$). To display better the differences between the FWHM of the various families, we calculate the ratio of the average FWHM_i for each family to the average FWHM_i for the (00·2) family; these "normalized" full width at half maximum (NFWHM) values are given in Table I under the heading, NFWHM_i, together with their estimated standard deviations derived from the single observation errors given above. Values of these ratios obtained from the three alternate unbroadening calculations mentioned earlier all are quite close to the values tabulated here, with the largest total spread among the four values for any ratio being only 1.2 times its tabulated standard deviation, which supports the reliability of these standard deviations, all less than 3%. The NFWHM data confirm that only the (10·3) family may have significantly different broadening along the $\vec{c}^*$ direction, and they demonstrate clearly the differences in broadening in the $\vec{a}^*$ direction shown by several of the families.

These are the data that are used for most of the following analysis of the structure of the ω phase in this alloy. The less precise measurements at earlier times are used only to examine its variation with time. Peak intensities are used here instead of the more usual integrated intensities, because the observed variations in peak breadth interfere with a straightforward interpretation of integrated intensities, as discussed in an earlier note.[29]

D. Other data

The displacements of some of the ω-phase peaks in this final set of measurements are given in Table II. The peak positions have been defined by the midpoints at $I=0.9I_\tau$; the slight profile asymmetries would yield somewhat larger values ($\leq 30\%$ greater) if measured from the midpoints at $I=0.5I_\tau$. The $\vec{c}^*$ displacements are all directed away from the nearest bcc RLP, just as McCabe observed, but the displacement magnitudes are much smaller—McCabe found displacements of $+0.018\vec{c}^*$ for the (00·1) and $-0.037\vec{c}^*$ for the (00·2) at this composition. The (00·2) displacement here, $-0.003\vec{c}^*$, corresponds to a scattering angle shift, $\Delta 2\theta=-0.11°$; for comparison, the displacement of the nearby (112) peak due to the misalignment effects is $\Delta 2\theta=+0.03°$. The precision of these $\vec{c}^*$ displacements is not high, but their small size and alternating sign pattern seem clearly established. Five of these peaks also show $\vec{a}^*$ displacements greater than $0.002|\vec{a}^*|$ that are considered significant; three of these are directed towards adjacent strong bridges, and two are directed away from the adjacent "missing" (30·2)-(04·$\bar{1}$) bridge. Similarly directed $\vec{a}^*$ displacements were noted in the data of Moss *et al.*[14] by Kuan and Sass.[18]

Measurements of the scattering near the (02·0) and (04·0) "forbidden reflection" RLP's, repeated for several sample orientations chosen to avoid multiple scattering effects, gave contour plots (e.g., Fig. 3) that show similar general features: Superposed on a varying background from nearby ω-phase peaks and bridges is a weak, ill-defined peak displaced from the (0k·0) RLP in the $+\vec{a}_2^*$ direction and a possible second, weaker peak displaced towards $-\vec{a}_2^*$. The peak intensity for the stronger member,

TABLE II. Final ω-phase peak displacements.

τ	Displacement	components
($\bar{1}$0·3)	$-0.002c^*$	$-0.004a_1^*$
($\bar{1}$0·2)	$+0.004c^*$	$+0.005a_1^*$
(00·2)	$-0.003c^*$	
(20·2)	$+0.006c^*$	$-0.015a_1^*$
(00·1)	$+0.004c^*$	
(10·1)	$-0.002c^*$	
(03·1)	$+0.004c^*$	$-0.013a_2^*$
(03·$\bar{1}$)	$-0.004c^*$	$-0.008a_2^*$

that displaced towards $+\vec{a}_2^*$, is ~ 0.3 counts/sec above background for both the (02·0) and (04·0), which, converted to the intensity units of Table I, corresponds to values of 0.0014 and 0.0034, respectively. The weaker member, more visible for the (04·0), shows an intensity $\sim 30\%$ of the stronger one.

After the final ω-phase peak measurements were completed, integrated intensities of the sets of β-phase reflections in the accessible region [(110) through (400)] were measured using two sizes of large receiver slits and both Ω and $\theta{:}2\theta$ scans. The combined results, corrected for atomic scattering factor and Lorentz polarization terms, show a large apparent attenuation $[E(400)=0.18E(110)]$ and departures from a smooth curve plot, similar to the Zr-Nb observations of Keating and LaPlaca.[7]

IV. ANALYSIS

A. General

An estimate of the dimensions of the average ω-phase particle can be obtained from the average FWHM_c and FWHM_a of the (00·2) family using the Keating-LaPlaca[7] cylindrical particle formulas. One finds a length of $\sim 26\,|\vec{c}\,|$ (73 Å) and a diameter of $\sim 10\,|\vec{a}\,|$ (46 Å), which gives a particle cross section of ~ 91 unit cells.

It is generally accepted[7] that athermal ω-phase particles remain coherent with their surroundings up to large particle sizes, based on electron microscope observations of delta fringes, strain field contrast, and an absence of misfit dislocations.[21] We suggest that the coherency of the ω-phase particles in our alloy is confirmed by the shape of the scattering contours around the β-phase RLP's. There is strong interference in the scattering from coherent ω-phase variants in a region very near a β-phase RLP, but the anisotropy of the constant intensity contours for each variant should cause the intervariant interference to decrease rapidly enough with increasing distance that the outer scattering contour around a β-phase RLP represents approximately a superposition of intensities from the four ω-phase variants, regardless of coherence. Now the ω-phase structure factor F is the same for both coherent and incoherent particles at *isolated* ω-phase RLP's, but there can be large differences between coherent and incoherent F's (and thus intensities) for ω-phase RLP's coincident with β-phase RLP's. For example, at the (222) the coincident ω_I RLP is the (00·3), while the coincident RLP for each of the other three variants is the (04·1); and for a range of parameter values appropriate to our alloy, for a *coherent* particle the (00·3) intensity is more than 10 times greater than the (04·1), while for an *incoherent* particle the (04·1) is almost 10 times greater than the (00·3).[30] The observed contour (see Fig. 1) around the (222) is very similar to contours around isolated $\omega_{\rm I}$ RLP's, e.g., the $(\bar{1}0\cdot 3)$, indicating that the $\omega_{\rm I}$ peak [the (00·3)] is dominant here, confirming the ω-phase particle coherence. Similar ω_I dominance for coherent particles is also predicted and seen for the contour around the (112), while at other β-phase RLP's within our range no single variant dominates and the observed contours show the superposition of several peaks. Our interpretation of these contours around β-phase RLP's as small particle scattering is supported by a comparison of calculated and estimated intensities relative to adjacent $\omega_{\rm I}$ peaks. Borie's recent calculation[31] for a complex, coherent model also supports our analysis, in that his calculated interference effects do not appear to affect significantly the outer contours around the (112) or (222) RLP's. Such contour shapes have not been noted previously,[11,14] perhaps because of poorer instrumental resolution.

B. Structure factor models

Our primary objective is to obtain a description of the structure of the ω phase in this alloy from our measured peak intensity and FWHM data. We try first the usual structure factor approach, in which the ω-phase particle is assumed to be formed of identical average unit cells, each having an A site at (0,0,0), unshifted by the transformation, and sites B and B' at $(\frac{1}{3},\frac{2}{3},\frac{1}{3}+\frac{1}{6}\delta)$ and $(\frac{2}{3},\frac{1}{3},\frac{2}{3}-\frac{1}{6}\delta)$, respectively, where δ, the parameter specifying the ω-phase displacement, can vary between 0 (untransformed bcc) and 1 (the final, perfect AlB_2 structure). Then, assuming a random atomic distribution and letting T_n represent the temperature factor (including both static and dynamic terms) for atoms on site n, the coherent structure factor for this average unit cell can be written as

$$
\begin{aligned}
(F/f) &= \sum_{n=1}^{3} \left(T_n e^{i\vec{K}\cdot\vec{r}_n} - T_0 e^{i\vec{K}\cdot\vec{r}_n^{\,0}}\right)\\
&= e^{i\pi(h_1+h_2+h_3)} \times \left\{ \begin{array}{l} (T_B+T_{B'})\cos\{\frac{1}{3}\pi[h_1-h_2+h_3(1-\delta)]\} - 2T_A\cos[\frac{1}{3}\pi(h_1-h_2+h_3)] \\ -i(T_B-T_{B'})\sin\{\frac{1}{3}\pi[h_1-h_2+h_3(1-\delta)]\} \end{array} \right\}\\
&\quad + (T_A-T_0)\{1+e^{i\pi(h_1+h_2+h_3)}2\cos[\tfrac{1}{3}\pi(h_1-h_2+h_3)]\}\ ,
\end{aligned}
$$

where f is the average atomic scattering factor, $\vec{r}_n^{\,0}$ locates the untransformed site n, T_0 is the average temperature factor for sites outside the ω-phase particle, and h_1, h_2, and h_3 are the hexagonal reciprocal space variables whose integral values are the ω-phase RLP Miller indices. The last term, with coefficient (T_A-T_0), is zero *at* each ω-phase RLP not coincident with a β-phase RLP, and we assume it can be neglected within the small region around a RLP containing the observed ω-phase peak. The coherent structure factor for these noncoincident ω-phase peaks then can be written

$$
\begin{aligned}
|F/f| \simeq{} & (T_B+T_{B'})\cos\{\tfrac{1}{3}\pi[h_1-h_2+h_3(1-\delta)]\} - 2T_A\cos[\tfrac{1}{3}\pi(h_1-h_2+h_3)]\\
& -i(T_B-T_{B'})\sin\{\tfrac{1}{3}\pi[h_1-h_2+h_3(1-\delta)]\}\ . \qquad (2)
\end{aligned}
$$

Following Borie[32] we write the temperature factor for atoms on site s as

$$T_s = \exp(-\tfrac{1}{2}\langle(\vec{\mathrm{K}}\cdot\vec{\mathrm{u}})^2\rangle_s)[1 - i\tfrac{1}{6}\langle(\vec{\mathrm{K}}\cdot\vec{\mathrm{u}})^3\rangle_s + \cdots] \\ = e^{-M_s}(1 - iD_s + \cdots)\ . \tag{3}$$

Let the instantaneous displacement of an atom from its equilibrium position be written as

$$\vec{\mathrm{u}} = x\vec{\mathrm{a}}_1 + y\vec{\mathrm{a}}_2 + z\vec{\mathrm{c}}\ .$$

The $3m$ symmetry of the B and B' sites reduces their quadratic terms to

$$M_B = M_{B'} = 2\pi^2\langle x^2\rangle_B(h_1^2 + h_1h_2 + h_2^2) + 2\pi^2\langle z^2\rangle_B h_3^2 \\ = B_{xx}(h_1^2 + h_1h_2 + h_2^2) + 2B_{zz}h_3^2 \tag{4}$$

where, for isotropy, $B_{xx} = B_{zz}$.

The $\bar{3}m$ symmetry of the A sites leads to exactly the same reduction,

$$M_A = A_{xx}(h_1^2 + h_1h_2 + h_2^2) + 2A_{zz}h_3^2\ , \tag{5}$$

where the parameters A_{ii} are directly analogous to the parameters B_{ii} of Eq. (4). Similarly, the $3m$ symmetry of the B and B' sites reduces their third-order terms to the following:

$$D_B = -D_{B'} = \frac{4\pi^3}{3}[\langle x^3\rangle_B(h_1^3 + \tfrac{3}{2}h_1^2h_2 - \tfrac{3}{2}h_1h_2^2 - h_2^3) + \langle x^2z\rangle_B 3h_3(h_1^2 + h_1h_2 + h_2^2) + \langle z^3\rangle_B h_3^3] \\ = \Delta_{xxx}(h_1^3 + \tfrac{3}{2}h_1^2h_2 - \tfrac{3}{2}h_1h_2^2 - h_2^3) + \Delta_{xxz}3h_3(h_1^2 + h_1h_2 + h_2^2) + \Delta_{zzz}h_3^3\ . \tag{6}$$

The $\bar{3}m$ symmetry of the A sites causes its odd-order terms to vanish.

Then, neglecting terms of fourth or higher order, the coherent structure factor for noncoincident ω-phase peaks can be written

$$|F/f| \simeq 2\times\left\{\begin{matrix} e^{-M_B}\cos\{\tfrac{1}{3}\pi[h_1 - h_2 + h_3(1-\delta)]\} - e^{-M_A}\cos[\tfrac{1}{3}\pi(h_1 - h_2 + h_3)] \\ -D_B e^{-M_B}\sin\{\tfrac{1}{3}\pi[h_1 - h_2 + h_3(1-\delta)]\} \end{matrix}\right\}\ , \tag{7}$$

where M_B, M_A, and D_B are given by Eqs. (4), (5), and (6), respectively.

If the temperature factors for all three sites are equal, so that $M_A = M_B = M$, and $D_B = 0$, Eq. (7) reduces to

$$|F/f| \simeq 4e^{-M}\sin\{\tfrac{1}{3}\pi[h_1 - h_2 + h_3(1 - \tfrac{1}{2}\delta)]\}\sin(\tfrac{1}{6}\pi\delta h_3) \tag{8}$$

and the procedure of comparing intensities of symmetrical pairs of reflections [e.g., the $(\bar{1}0\cdot3)$ and $(10\cdot3)$] suggested by several investigators[6,11] can properly yield a value of δ independent of the Debye-Waller exponent M. However, if $M_A \neq M_B$ and/or $D_B \neq 0$, that procedure is not valid, and a solution for δ from intensity data requires using the general structure factor expression, Eq. (7), and solving also for M_A, M_B, and D_B.

We have written an iterative, nonlinear least-squares-fitting program to match the 15 final peak intensities P_i given in Table I to calculated quantities, $Q_i = k\,|F/f|^2$, where k is a scale factor and $|F/f|$ is given by Eq. (7), to obtain values for k, δ, and the harmonic and anharmonic parameters [see Eqs. (4)–(6)] for models with various restrictions. In the fitting, each $(P-Q)_i^2$ is weighted inversely as σ_i^2 using the estimated σ_i values given in Table I. The goodness of fit between observed and calculated intensities for a given model is measured by the quantity

$$\Delta_{(P-Q)^2} = \frac{1}{14-n}\sum_i^{15}\left[\frac{(P-Q)}{\sigma}\right]_i^2\ , \tag{9}$$

where n is the number of variable parameters; a value of $\Delta_{(P-Q)^2}$ close to unity indicates that the σ_i have been correctly evaluated and that the model is reasonable. The calculations were carried out on a Hewlett-Packard HP-9830A table-top calculator to yield convergence through four to five digits.

The simplest model—isotropic $M_A = M_B$, and harmonic ($D_B = 0$)—is the one usually assumed, along with Eq. (8). Using Eq. (8) and either the $(\bar{1}0\cdot3)$-$(10\cdot3)$ or the $(20\cdot3)$-$(\bar{2}0\cdot3)$ pairs of intensities, we find $\delta = 0.80$. Fitting all 15 peaks with this three-parameter model gives $\delta = 0.847 \pm 0.018$, in fair agreement with the Eq. (8) solution. However, the fit to the set of peaks is very poor, with $\Delta_{(P-Q)^2} = 374.3$ and with a maximum intensity discrepancy $(P-Q)_m \simeq 58\%$.

A second model—anisotropic $M_A = M_B$, and $D_B = 0$—also gives $\delta = 0.847 \pm 0.018$; again the fit is very poor: $\Delta_{(P-Q)^2} = 409.0$ and $(P-Q)_m \simeq 52\%$. Another four parameter model—isotropic M_A, isotropic M_B, and $D_B = 0$—gives $\delta = 0.770 \pm 0.027$; the fit is improved, but still quite poor: $\Delta_{(P-Q)^2} = 152.7$ and $(P-Q)_m \simeq 42\%$.

The five-parameter model—isotropic M_A, *anisotropic* M_B, and $D_B = 0$—gives a dramatic improvement in fit: $\Delta_{(P-Q)^2} = 12.45$, and $(P-Q)_m \simeq 10\%$. The parameter values and their calculated standard deviations are given

TABLE III. Parameters for structure-factor models.

Model	5	6	7A	7B
A_{xx}	0.0136±0.0024	0.0152±0.0018	0.0140±0.0012	0.0194±0.0013
A_{zz}			0.0196±0.0015	
B_{xx}	0.0170±0.0021	0.0185±0.0016	0.0170±0.0011	0.0234±0.0014
B_{zz}	0.0744±0.0017	0.0824±0.0028	0.0896±0.0026	0.0903±0.0025
Δ_{zzz}		−0.0166±0.0058	−0.0284±0.0052	−0.0316±0.0056
Δ_{xxz}				−0.0011±0.0003
δ	0.309±0.023	0.351±0.016	0.346±0.008	0.346±0.008
$\Delta_{(P-Q)^2}$	12.45	6.98	2.85	2.49

as model 5 in Table III. One should note the large anisotropy of M_B. The anisotropic M_B is the key factor in this improved fit; an alternate five-parameter model—anisotropic M_A, isotropic M_B, and $D_B=0$—gives $\delta=0.740\pm0.041$ and a quite poor fit: $\Delta_{(P-Q)^2}=146.3$ and $(P-Q)_m\simeq37\%$.

Although model 5 offers a major improvement over the simpler models, its overall fit to the data and 10% maximum discrepancy [for the strong (00·2) peak] are not satisfactory, and the remaining harmonic model, with both M_A and M_B anisotropic, gives no improvement, so anharmonicity for the B and B' site atoms must be included. For the simplest anharmonic model we add to model 5 one third-order parameter, Δ_{zzz}, keeping Δ_{xxz} and Δ_{xxx} fixed at zero. This model gives a significantly better fit: $\Delta_{(P-Q)^2}=6.98$ and $(P-Q)_m\simeq6\%$ [for the (00·1)]. The parameter values are listed as model 6 in Table III. The large anisotropy of M_B persists, and there is a significant negative value for Δ_{zzz}.

Two seven-parameter anharmonic models offer much better fits. Model 7A, which is model 6 changed to allow an anisotropic M_A, gives $\Delta_{(P-Q)^2}=2.85$, $(P-Q)_m\simeq6\%$ [for the weak (20·2)], and all other $(P-Q)_i\leq4\%$. Model 7B, which is model 6 plus another third-order parameter, Δ_{xxz}, gives $\Delta_{(P-Q)^2}=2.49$, $(P-Q)_m\simeq7.5\%$ [for the (20·2)], and all other $(P-Q)_i\leq4\%$. These are the first acceptable fits to our data. The parameters for these two models are listed in Table III. Both models show a large anisotropy for M_B and a large negative value for Δ_{zzz}.

A number of other models were explored, but none offered any real improvement over models 7A and 7B. Several observations from these trials should be noted: (1) The other third-order parameter, Δ_{xxx}, is an order of magnitude smaller than Δ_{xxz} and not significant; the anharmonic term is very anisotropic, with Δ_{zzz} dominant. (2) Although the third-order anharmonic term is important here, a fourth-order term is not needed—models with the temperature factor [Eq. (3)] extended to include the next-higher term give fitted combined fourth-order parameters less than or equal to one standard deviation and thus not significant. (3) Model 7A is exceptional as the only one among four models allowing an anisotropic M_A actually to yield parameter values giving M_A a significant anisotropy. (4) Ten of our ω-phase peaks are from the ω_{I} variant and five are from the ω_{II} variant, which we have assumed to be present in equal amounts; that assumption is verified by models with separate scale factors for the two sets of peaks, whose fitted values have the ratio, $k_{\mathrm{I}}/k_{\mathrm{II}}=1.02\pm0.10$. (5) A search for alternate solutions for model 7B arising from the nonlinearity of the fitting process, by trying a wide range of initial parameter values in the program, yielded four much poorer solutions, the best of which gave $\Delta_{(P-Q)^2}=51.0$ and $(P-Q)_m\simeq23\%$; the parameters in Table III do represent the best solution for this model.

Models 7A and 7B both give a reasonable fit to the observed intensities of Table I. We now try to find a particle size and shape which, together with the structure factors for these models, will give calculated FWHM values to match the observed FWHM data of Table I. The different families of reflections show different FWHM values, particularly in the FWHM$_a$ data, and the problem is to match the data for all six families. We shall focus primarily on trying to match the NFWHM$_a$ data, which display better the differences between families.

Programs have been written to calculate the scattering from an isolated particle made up of a regular array of

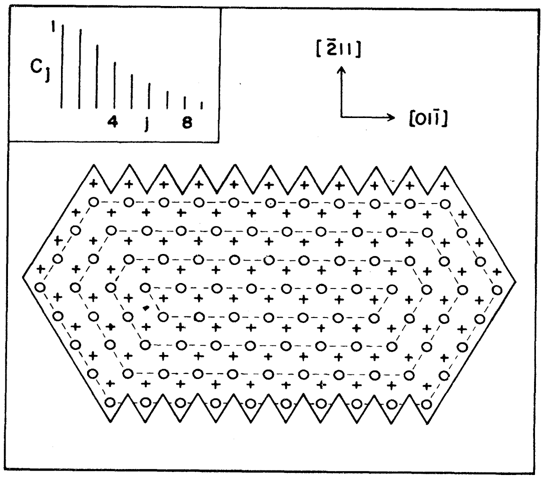

FIG. 5. Cross section, one-cell thick, of multisite ω-phase particle model F, with an area of 96 unit cells. The $\vec{c}$ axis, parallel to [111], is up normal to the plane. Circles and crosses denote atoms displaced, respectively, upwards and downwards from bcc positions by the transformation; the undisplaced atoms, at cell corners, are not shown. Dashed lines link the atoms in a set that have a common upwards displacement, and these sets alternate radially with sets of atoms with a common downwards displacement. The inset shows the relative displacements c_j for the nine different sets, normalized in terms of the displacement for the innermost set of seven atoms, that were appropriate for model FQB, discussed later in the text.

uniform unit cells, using the coherent structure factor of Eq. (7) and the parameters of models 7A or 7B. The particle has the form of a short rod, $25\,|\vec{c}\,|$ in height, with a uniform six-sided cross section (see Fig. 5) whose dimensions (particularly the serrated edge) have been altered in different programs to give shape anisotropies (mean width to thickness ratio) ranging from 1.07 to 2.43. It is assumed that such particles occur in the crystal with equal probability in each of the three equivalent orientations about the [111] axis but separated by such varying steps of $\vec{a}_1$, $\vec{a}_2$, and $\vec{c}$ as to eliminate interparticle interference, so the total intensity is calculated as an average of the intensities for each of the three orientations. Then, by calculating profiles along the $\vec{a}^*$ direction through the different ω-phase peaks, we can derive the set of NFWHM$_a$ values for each model and particle shape.

Sets of NFWHM$_a$ values have been calculated for six different particle cross sections for both model 7A and 7B parameters. The results for a given particle using models 7A and 7B are almost indistinguishable, with a maximum NFWHM$_a$ difference of only 0.3%. The model 7A results for three particles spanning the range of shape anisotropies are given in Table IV. One notes that only the (10·3) and ($\bar{1}$0·2) families show any appreciable shape dependence. A comparison of these results with the observed NFWHM$_a$ values in Table I shows two major differences that persist for all shapes: the calculated (00·1) value is much smaller than that observed; and the calculated ($\bar{1}$0·2) is much larger than the calculated (10·3), while the observed NFWHM$_a$ show the (10·3) to be slightly the larger. Two further calculations for particles with some tapering at the ends gave no improved agreement. We conclude that, while it can give an acceptable fit to the observed intensities, the structure factor model cannot match the observed FWHM data and thus cannot offer a valid description of the ω-phase in our alloy.

C. Multisite models

The structure factor model treats the ω-phase displacements as being uniform throughout the particle. The average particle diameter is only $\sim 10\,|\vec{a}\,|$, which suggests that particle boundary effects could be significant. Thus we have developed alternate, multisite models of an ω-phase particle in which the displacement can vary with position in the particle, decreasing as the boundary is neared. We consider an isolated, coherent particle, whose "unit cells" have an unshifted A site at (0,0,0) and displaced sites B and B' at $(\frac{1}{3},\frac{2}{3},\frac{1}{3}+\frac{1}{6}\delta_j)$ and $(\frac{2}{3},\frac{1}{3},\frac{2}{3}-\frac{1}{6}\delta_k)$, respectively, formed as before as a short rod with possible tapered ends and with uniform, six-sided central cross sections whose shape anisotropy in different programs ranges from 1.07 to 2.43. The number of distinguishable displacements δ_i is kept to a manageable level by specifying that a set of sites defined by location relative to the boundaries all have equal displacements. For example, Fig. 5 shows a one-cell-thick cross section of multisite model F, which has an area of 96 unit cells and a shape anisotropy of 1.95. The $\vec{c}$ axis extends up normal to the plane. B sites, with upward displacements, are indicated with circles, and B' sites, with downward displacements, by crosses; the undisplaced A sites, at cell corners, are not shown. Dashed lines link the B sites in a set that have a common displacement, and these sets alternate radially with sets of B' sites. The 192 displacive sites in this cross section are thus divided into a central, linear set of seven B' sites with displacement δ_1, surrounded successively by 15 B sites with δ_2, then 18 B' sites with δ_3, etc., ending with an outer incomplete ring of 14 B' sites with displacement δ_9. In the analyses only the largest displacement, δ_1, is evaluated as an independent variable, with a set of constants c_j, fixing the relative sizes of the other displacements, $\delta_j = c_j\delta_1$. A plot of one set of relative displacements c_j is shown in the inset of Fig. 5. The usual model particle is composed of 25 such layers, capped at either end with one layer having reduced displacements to give crude tapering, this being called a 1-25-1 distribution. Other distributions with more extended tapering have also been tried.

TABLE IV. Calculated structure-factor model 7A NFWHM$_a$ values vs particle-shape anisotropy for the different ω-phase peak families.

Anisotropy	1.07	2.08	2.43
(10·1)	0.999	0.998	0.998
($\bar{1}$0·3)	1.002	1.004	1.003
(00·1)	1.008	1.018	1.018
(10·3)	1.070	1.197	1.226
($\bar{1}$0·2)	1.297	1.678	1.779

The scattered amplitude from the multisite model particle can be written

$$E/f = \sum_{B,B'} \left(T_n e^{i\vec{K}\cdot\vec{r}_n} - T_A e^{i\vec{K}\cdot\vec{r}_n^{\,0}}\right) + (T_A - T_0)\sum_{\text{all}} e^{i\vec{K}\cdot\vec{r}_n^{\,0}} ,$$

where the first term is a sum over just the B and B' sites, with $\vec{r}_n - \vec{r}_n^{\,0} = +\frac{1}{6}\delta_n\vec{c}$ for B sites and $-\frac{1}{6}\delta_n\vec{c}$ for B' sites, and where T_A is assumed to be independent of site. The last term, with coefficient $(T_A - T_0)$, is zero *at* each ω-phase RLP not coincident with a β-phase RLP, and we assume as before that it can be neglected within the small region around a RLP containing the ω-phase peak. The scattered amplitude for these noncoincident peaks can then be written

$$E/f \simeq \sum_{B,B'} \left(T_n e^{i\vec{K}\cdot\vec{r}_n} - T_A e^{i\vec{K}\cdot\vec{r}_n^{\,0}}\right) . \tag{10}$$

We adopt Borie's temperature factor form, Eq. (3), and we assume that we can still use $3m$ symmetry for B and B' sites and $\bar{3}m$ symmetry for A sites to reduce the harmonic and anharmonic terms, so that Eqs. (4)—(6) still apply. We note that the variation of δ_j in the particle suggests that the harmonic and/or anharmonic parameters for the B and B' sites may also vary with position through a dependence on δ_i.

We have written iterative, nonlinear least-squares-fitting programs to match the 15 final peak intensities P_i to calculated intensities, $Q_i = k\,|E/f\,|_i^2$, using Eq. (10) for multisite particles of the six different cross sections considered earlier, using a given set of relative displacements c_j and a given layer distribution. The approach is the same as in the structure factor programs, with the same weights and goodness-of-fit measure, and the calculations are carried out to a similar precision. The parameters evaluated are the scale factor k, the harmonic and anharmonic parameters for a given model (the maximum parameter value if there is a dependence on δ_j), and the inner, maximum displacement, δ_1.

We have also written programs to calculate the scattering from an isolated multisite particle of each of these six cross sections using Eq. (10) and the various relative displacements and parameters appropriate to a given model. As before, the intensity is calculated as an average of the intensities for the three equivalent orientations about the [111] axis, neglecting interparticle interference. Then, from calculated profiles along the $\vec{a}^*$ and $\vec{c}^*$ directions through the ω-phase peaks we derive the complete set of FWHM values for each model.

Calculations have been made for multisite particles of two cross sections (anisotropies of 1.09 and 1.95) and different sets of relative displacements ($\langle c_j \rangle = 0.40$ and 0.50) to examine the fit to the intensities that can be obtained for the various temperature factor models. In each case the results are very similar to those for the structure factor fits: No harmonic model gives a good fit; the first models to give an acceptable fit are models 7A and 7B, which both show an anisotropic M_B and a large negative Δ_{zzz}; and inclusion of fourth-order anharmonic parameters, tested in several cases, yields combined fourth-order terms that are not significant. Thus the remainder of the analysis is limited to using temperature factor models 7A and 7B.

Our objective is to find model particles that can give a reasonable fit both to the intensities and the FWHM data. Calculations for a variety of models, including different cross sections, different sets of relative displacements c_j, and some differences in the dependence of the harmonic and anharmonic parameters on δ_j, show that the fit to the intensities is insensitive to most of these factors—the values of some parameters change somewhat, but the overall fit stays almost the same—so the problem reduces to finding models that can fit the FWHM data. The calculated FWHM show varied responses to these factors—for example, as the relative displacements c_j are made to decrease more steeply with increasing j, the stronger changes in NFWHM$_a$ generally are a decrease for the $(\bar{1}0{\cdot}2)$ peak and increases for the $(10{\cdot}3)$ and $(00{\cdot}1)$ peaks—and the search for a fit to the observed data has involved calculations for a considerable number of models.

TABLE V. Calculated FWHM and NFWHM values for model *FQB*.

τ	NFWHM$_c$	NFWHM$_a$
$(10 \cdot 1)$	1.003	1.048
$(\bar{1}0 \cdot 3)$	0.996	0.937
$(00 \cdot 1)$	1.004	1.110
$(10 \cdot 3)$	1.000	1.253
$(\bar{1}0 \cdot 2)$	0.980	1.209

$(00{\cdot}2)$: FWHM$_c = 0.0340\,|\vec{c}^*|$, FWHM$_a = 0.0907\,|\vec{a}^*|$.

We have found five models that give approximately equal, reasonable fits to the observed intensity and FWHM data. The calculated FWHM data for one of these, model *FQB*, are shown in Table V. The agreement of the NFWHM$_a$ values with experiment is much improved over that for the structure factor models; in fact, the largest discrepancy here is in the NFWHM$_c$ for the $(10{\cdot}3)$, suggesting a need for improved tapering at the ends. Parameters for these five models are given in Table VI. The letters designating the model indicate the following: F is the cross section F (Fig. 5), with shape anisotropy of 1.95; G is the cross section G (wider and thinner than F), with shape anisotropy of 2.43; A (or B) is the temperature factor model 7A (or 7B); Q shows that the anharmonic parameters are position dependent, with $\Delta_j = \Delta[4\delta_j(1-\delta_j)]$, where Δ is the tabulated maximum value; and X shows that the harmonic terms for B and B' sites are position dependent, with $M_j = yM_B + (1-y)M_A$, where $y = (c_j)^{1/8}$ and M_B and M_A are the limiting tabulated values. All models have a 1-25-1 layer distribution, giving only slight tapering. The set of relative displacements, c_j, for model *FQB*, with $\langle c_j \rangle = 0.39$, are plotted in the inset of Fig. 5; those for *FQA* and *FQXB* are fairly similar, while those for *FA* and *FB*, with $\langle c_j \rangle = 0.50$, decrease more linearly to zero. The fit between the calculated and observed FWHM [for the $(00{\cdot}2)$] and NFWHM data is measured by the quantity, $\Delta_{\epsilon^2} = \frac{1}{12}\sum_i (\epsilon_i/\sigma_i)^2$, where ϵ_i is the difference between the ith observed and calculated value and σ_i is its tabulated standard deviation. The fit of these models to the intensities, measured by $\Delta_{(P-Q)^2}$, is seen to be very similar to that achieved with the structure factor models, confirming the insensitivity of this fit noted earlier. The fit of these models to the FWHM data is not as good as the intensity fit, but further model refinement does not seem worthwhile. The parameters for each model show an anisotropic M_B and a large negative Δ_{zzz}. For each model the inner, maximum dis-

TABLE VI. Parameters for multisite models fitting the final intensity and FWHM data.

Model	*FA*	*FB*	*FQA*	*FQB*	*GQXB*
A_{xx}	0.0140 ± 0.0012	0.0193 ± 0.0012	0.0141 ± 0.0012	0.0221 ± 0.0015	0.0225 ± 0.0014
A_{zz}	0.0195 ± 0.0014		0.0218 ± 0.0018		
B_{xx}	0.0171 ± 0.0011	0.0233 ± 0.0014	0.0171 ± 0.0011	0.0261 ± 0.0016	0.0272 ± 0.0016
B_{zz}	0.0777 ± 0.0027	0.0795 ± 0.0026	0.0739 ± 0.0028	0.0749 ± 0.0026	0.0820 ± 0.0026
Δ_{zzz}	-0.0285 ± 0.0053	-0.0317 ± 0.0056	-0.0418 ± 0.0085	-0.0445 ± 0.0081	-0.0502 ± 0.0087
Δ_{xxz}		-0.0011 ± 0.0003		-0.0022 ± 0.0005	-0.0024 ± 0.0005
δ_1	0.697 ± 0.017	0.675 ± 0.015	0.840 ± 0.044	0.799 ± 0.031	0.789 ± 0.027
$\Delta_{(P-Q)^2}$	2.84	2.49	2.80	2.48	2.35
Δ_{ϵ^2}	1.43	1.68	1.69	1.74	1.91

placement δ_1 is large, approximately 75% of a complete ω-phase shift, while the average displacement, $\langle \delta_j \rangle = \delta_1 \langle c_j \rangle$, is only approximately $\frac{1}{3}$. The tabulated error in a parameter, derived in the least-squares fitting, is meaningful only within the assumption of a particular model and in several cases does not match the spread in values among the different models. Two points should be noted.

(1) The multisite models that fit the FWHM data all have anisotropic cross sections, with shape anisotropies $\gtrsim 2$. For comparison, the best FWHM fit we obtained for a particle of almost equiaxed cross section (shape anisotropy of 1.09) gives $\Delta_{\epsilon^2} = 2.83$, with calculated NFWHM$_a$ values $\simeq 10\%$ too small for both the (10·3) and ($\bar{1}$0·2) families.

(2) The multisite models that fit the data share several other characteristics—anisotropic M_B, large negative Δ_{zzz}, large δ_1—but they also display appreciable differences in their relative displacements c_j and in the position dependence of their anharmonic (const vs Q) and harmonic (const vs X) terms. This diversity of acceptable models prevents any more detailed, quantitative description of the average ω-phase particle in our alloy.

D. Time dependence

Model *FQB* has been used to analyze the five less-accurate sets of ω-phase intensities measured at earlier times during the 14-month period (see Fig. 4) to investigate the time dependence of the various parameters. A least-squares fit was made to each set of intensities, using approximate errors reflecting the less accurate nature of the data, with the relative displacements c_j being adjusted slightly as needed to improve the fit to the time-independent FWHM values. The fit to these earlier sets of intensities is comparable to that obtained for the final intensities, with only the earliest, least-accurate set giving a noticeably poorer match. The results suggest that three parameters—the scale factor k (proportional to the fraction of alloy transformed), the harmonic parameter B_{zz}, and the magnitude of the anharmonic parameter Δ_{zzz}—increase asymptotically with time, with a total change from initial to final values amounting to 20% for k, 5.4% for B_{zz}, and 22% for $|\Delta_{zzz}|$, half of this occurring in the two months between the first and second measurements. These total changes, in units of the average error of a parameter, amount to 2.0σ for k, 1.2σ for B_{zz}, and 0.9σ for Δ_{zzz}, so quantitative statements are not reliable. No trends were evident for the other parameters.

E. Fraction transformed

The final set of ω-phase peak intensities has been combined with the integrated intensities of the eight accessible β-phase reflections in evaluating the fraction of the alloy that has transformed into ω phase. The treatment of the β-phase integrated intensities follows the approach of Keating and LaPlaca,[7,33] but uses model *FQB* to describe the average ω-phase particle. The expression for the integrated intensity is cumbersome and will not be reproduced here; it involves all the parameters used for the ω-phase peak intensities (except the scale factor k), plus a second scale factor, an isotropic extinction parameter, an isotropic, harmonic β-phase site temperature factor parameter C_0, and the volume fraction transformed x_0. The nonlinear least-squares-fitting program has been expanded to match the 15 ω-phase peak intensities and the eight integrated intensities, with all parameters except C_0 as independent variables (C_0 and x_0 are strongly correlated; a restriction on C_0 allows convergence to be established). With the restriction that the β-phase site and A site temperature factors are equal (i.e., $C_0 = A_{xx} = A_{zz}$), the resulting fit yields values for the various temperature factor parameters and the displacement δ_1 that are within one standard deviation of the values obtained fitting just the ω-phase peak data, and the fraction transformed is given as $x_0 = 0.89 \pm 0.14$. If we assume instead that C_0 is some percentage larger than $A_{xx} = A_{zz}$, the value for x_0 is increased. If we repeat the calculation with model *FB* rather than *FQB* for the average ω-phase particle, again assuming $C_0 = A_{xx} = A_{zz}$, the ω-phase particle parameters again repeat satisfactorily, and the fraction transformed is found to be $x_0 = 0.93 \pm 0.11$. We conclude that at the time of the final measurements the alloy has almost completely transformed into the ω phase.

F. Unresolved points

No satisfactory explanation of the ω-phase peak $\vec{c}^{\,*}$ displacements has been found. Each displacement shifts the ω-phase peak away from the nearest β-phase RLP, which is the result expected for a subvariant stacking sequence, $\omega_1 \rightarrow \omega_3 \rightarrow \omega_2$, as noted by Borie *et al.*,[17] but the displacement magnitudes calculated from a model with that stacking and the observed total particle length are an order of magnitude larger than those observed. The ω-phase peak $\vec{a}^{\,*}$ displacements appear similar to (but much smaller than) those derived by Kuan and Sass[18] by including in their particle model some ω-phase displacement components perpendicular to $\vec{c}$. We have not tried to include such components in our models.

Diffuse bridges or streaks found in other studies generally have been interpreted in terms of linear ω-phase-like particles of a small cross section, with curvature arising from intervariant interactions[23,34] or from a particular model of the displacement field.[35] The differences in bridge shapes and intensities found here have not been given a satisfactory interpretation. Our few attempts to treat intervariant interactions were unsuccessful.

The very weak, "forbidden" (0k·0) reflections show $\vec{a}^{\,*}$ displacements and possible asymmetric doubling. We can suggest several possible origins for nonzero (0k·0) intensities—the difference between M_B and M_A, which for model *FB* seems to give (02·0) and (04·0) intensities within a factor of 3 of those observed; ordering of the V atoms on A sites, which could give comparable intensities; and ω-phase displacements $\vec{\delta}$ with components perpendicular to $\vec{c}$—but we can offer no detailed interpretation of the observations.

Finally, we have no satisfactory explanation of the slow decrease of the lattice parameter a_0. The 0.018% total change in a_0 could be viewed as reflecting a change in the β-phase composition corresponding to an additional 0.24% of vanadium, but since the alloy has transformed almost completely into ω phase, this interpretation does not seem meaningful.

V. DISCUSSION

The measured scattering distribution from our quenched Ti-V alloy shows fairly sharp, crystalline ω-phase peaks characteristic of rodlike particles with an average volume of ~ 2500 unit cells. To study the structure of these particles, we have made accurate intensity and halfwidth measurements for 15 of these ω peaks. No comparable set of data for an athermal ω phase has previously been obtained. A complete set of halfwidths was needed, because of the unexpected discovery that some of the ω-phase peaks had significantly greater widths, particularly in the $\vec{a}^*$ direction. These anomalous widths complement the peak intensities as a second distinctive set of data to be matched in a structure analysis. Such extra broadening, which is generally to be expected for small particles and reflections with rapidly varying structure factors,[29] should occur for most quenched, imperfect ω phases. It has not been noted in any other study, probably because of poorer instrumental resolution.

Two other scattering observations warrant special mention: (a) the differing contour shapes around the various β-phase RLP's, which confirm the coherence of the ω-phase particles; and (b) the slow time dependence of the diffraction patterns, showing the ω-phase transformation continues to progress at room temperature until finally, 16 months after the quench, the alloy has almost completely transformed. Neither of these has been seen in prior studies, presumably because of poorer resolution and short measurement periods.

We have not been able to interpret satisfactorily a few other features of the patterns: the small ω-phase peak shifts, which differ from both previous peak shift observations; the diffuse bridges, in greater variety here; and the very weak, displaced $(0k\cdot 0)$ peaks. We believe that these are only peripheral features that are not important to our general conclusions.

The analysis to obtain a structural description of the average ω-phase particle has used both the peak intensities and the FWHM data. The analysis of the intensities yields one primary result: The set of intensities can be fit almost equally well by uniform structure factor models or by multisite models of various shapes and displacement distributions, where in all cases the temperature factor for the atoms displaced in the transformation has a very anisotropic quadratic term ($B_{zz} \approx 4B_{xx}$) and a large negative third-order anharmonic term, Δ_{zzz}. This same result is also obtained if we treat the ω-phase particle as incoherent with respect to its surroundings rather than coherent, or if we use the intensity data without the instrumental broadening correction—the parameter values vary somewhat among these cases, but the anisotropic, anharmonic temperature factor remains as a basic characteristic of the displacive ω-phase atoms. The variety of well-fitting models emphasizes a second point: One cannot evaluate the ω-phase displacements from peak intensities until a model of the ω-phase particle has been established by other means.

The FWHM data allow us to restrict appreciably the range of possible models for the average ω-phase particle. The FWHM ratios—the NFWHM data—have been shown to be quite insensitive to details of the instrumental broadening correction, their only significant correction, and we find that a reasonable fit to these NFWHM data can be achieved only for models with two characteristics: the models are multisite, with displacements δ_j varying from a maximum at the center to zero at the boundary, *not* uniform structure factor types; and the cross section of the rodlike model is anisotropic, with a mean width (along $[01\bar{1}]$) approximately twice the mean thickness (along $[\bar{2}11]$).

Five models have been found that give comparable, reasonable fits to the intensity and FWHM data. These models all show large central displacements, and they share the common characteristics discussed above, but they have appreciable differences in displacement distributions and in the position dependence of harmonic and anharmonic temperature factor terms and thus give a range of descriptions of the average ω-phase particle. The models with Q-type anharmonic terms $[\Delta_j \sim \delta_j(1-\delta_j)]$ seem more plausible, since in a uniform structure Δ is required by symmetry to vanish if $\delta_j = 0$ or 1, and the model with X-type quadratic terms seems to offer better boundary behavior, even though a $(c_j)^{1/8}$ dependence is rather weak,[36] but in modeling this complex, highly transformed alloy such selection arguments do not seem very strong.

The sizes of the different temperature factor terms for these models are better appreciated from an example. At the $(\bar{1}0\cdot 3)$ reflection model *FQB* gives $M_A = 0.420$, $M_B = 1.374$, and $D_B = -1.221[4\delta_j(1-\delta_j)]$. A single, isotropic, harmonic temperature factor for all atoms is obviously a very poor approximation. These terms depend strongly on the Miller index l of the peak, so the differences will be smaller for lower angle reflections. To complete the example, the next term in the expansion of T_B is the combined fourth-order term, $\frac{1}{24}\langle(\vec{K}\cdot\vec{u})^4\rangle - \frac{1}{8}\langle(\vec{K}\cdot\vec{u})^2\rangle^2$ which at the $(\bar{1}0\cdot 3)$ peak for a similar, fitted *FQB*-type model has the value, 0.24 ± 0.26, which can be ignored.

The temperature factor for the shifting atoms in these models is characterized by large values for B_{zz} and Δ_{zzz}, which are proportional to $\langle z^2 \rangle$ and $\langle z^3 \rangle$, respectively, where z is the $\vec{c}$ component of the "instantaneous" displacement of an atom from its average, shifted position. The $\vec{c}$ axis is also the direction of the displacement δ_j of an atom during the transformation from β to ω phase. We submit that these large temperature factor parameters, with both static and dynamic components, must result from the nature and progress of this ω-phase transformation, and, as a corollary, that one should expect to find similar temperature factors for any incomplete ω phase. The quantities, $(\langle z^2 \rangle)^{1/2}$ and $-(\langle z^3 \rangle)^{1/3}$, derived from these parameters for our five models all have approximately the same large average value, 0.52 (in the same units as δ), and for each model the specific value of either quantity at site j exceeds the corresponding value of δ_j for all but the three innermost sets of sites (i.e., for more than 75% of the shifted sites). The negative sign of Δ_{zzz} means that $(\langle z^3 \rangle)^{1/3}$ is directed oppositely to $\vec{\delta}$, i.e., back towards the former β-phase site of the atom. We find thus that over 75% of the shifted atoms in our average multisite particle have both rms and root-mean-cubed "instantaneous" displacements that can return the atoms to their original β-phase sites. We have no satisfactory interpretation of this result.

The anisotropic cross section gives the average particle shape as a thick rectangular platelet rather than a cylindrical rod, with the plane of the platelet parallel to a $\{11\bar{2}\}$ plane and its longer dimension along [111]. Its internal multisite structure consists basically of a stack of $\{11\bar{2}\}$ planes of atoms, where all atoms in one plane are displaced parallel to [111] by the same amount, with that displacement varying on consecutive planes as $\ldots, +\delta_i, -\delta_{i+1}, 0, \ldots,$ plus appropriate edge connections. This particle shape and internal structure correlate well with the $\{11\bar{2}\}$ plane glide model of the ω-phase transformation proposed by Hatt and Roberts[8] and do not support the more recent [111] longitudinal phonon condensation model of de Fontaine.[37]

de Fontaine *et al.*[23] sketched the idea of a multisite model, suggesting that when the ω-phase particles are small, the number of atoms in the strained β-ω interfacial region with less than complete ω-phase displacements will represent a significant fraction of the total number in the particle. The multisite model is required here for a particle with a 95 unit cell cross section. The displacement in our particle does not appear to attain the complete ω-phase shift in the center, the maximum displacement for the different models ranging between 0.68 and 0.84. This incomplete maximum value, and the steep decrease in displacement for sites closer to the boundaries, suggest that our particle represents a case in which the particle thickness is less than twice the effective depth of a strained interfacial zone. Extrapolating from this structure versus size hypothesis, we estimate that an ω-phase particle must have dimensions several times larger than those here (i.e., a volume $> 10^5$ unit cells) before its interfacial zone forms a negligible volume fraction of the particle and an average, perfect ω phase is achieved.

Our results have indicated that quenched, imperfect ω phases need both multisite models and anisotropic, anharmonic temperature factors for the shifting atoms to obtain an adequate, average particle description. Only two previous studies[17,18] have used other than uniform displacement structure factor models, and none have used anything more than a common isotropic, harmonic temperature factor, so no previous quantitative structural results can be accepted with any confidence.

Our analysis has been restricted to calculations for an isolated, average ω-phase particle, neglecting interference effects. Interference from different variants should be negligible for our individual ω-phase peaks, since the peaks are fairly sharp and have minimal overlap; and, though this interference can be strong at β-phase RLP's (see Borie[31]), we think it should not affect the general shape of their outer contours. Subvariant domains do not occur here with the ordered $\omega_1 \rightarrow \omega_3 \rightarrow \omega_2$ stacking sequence found in other alloys,[17] since the corresponding peak shifts would be much larger than those observed, and we think that the several orientations and varied separations in a random subvariant distribution should average out their interference effects on the ω-phase peaks.

The objective of this study has been to obtain a first detailed structural description of a quenched imperfect ω phase. The observation that ω-phase peaks show significantly different widths changed the approach from a conventional structure-factor—particle-size analysis into an investigation of particle models of various shapes and displacement distributions and of temperature factors of several forms, which led finally to several equally valid solutions. The common features of these solutions—the thick platelet shape, the generally steep multisite displacement distribution, and the anisotropic, anharmonic temperature factor for the shifting atoms—together with the ranges of parameter values, provide the most detailed description of this imperfect ω phase that we can offer. We suggest that multisite displacement distributions and anisotropic, anharmonic temperature factors must be primary characteristics of all quenched, imperfect ω phases.

ACKNOWLEDGMENT

We are indebted to Professor S. L. Sass for the single-crystal Ti-V sample, and to Dr. H. F. Priest for much invaluable support.

---

[1] B. S. Hickman, J. Mater. Sci. 4, 554 (1969).

[2] S. L. Sass, J. Less-Common Met. 28, 157 (1972).

[3] J. M. Silcock, M. H. Davies, and H. K. Hardy, *Symposium on the Mechanism of Phase Transformations in Metals* (Institute of Metals, London, 1956), p. 93.

[4] J. M. Silcock, Acta Metall. 6, 481 (1958).

[5] Iu. A. Bagariatskii, G. I. Nosova, and T. V. Tagunova, Doklad. Akad. Nauk. SSSR 105, 1225 (1955).

[6] Iu. A. Bagariatskii and G. I. Nosova, Kristallografiya 3, 17 (1958) [Sov. Phys.—Crystallogr. 3, 15 (1958)].

[7] D. T. Keating and S. J. LaPlaca, J. Phys. Chem. Solids 35, 879 (1974).

[8] B. A. Hatt and J. A. Roberts, Acta Metall. 8, 575 (1960).

[9] D. J. Cometto, G. L. Houze, Jr., and R. F. Hehemann, Trans. Metall. Soc. AIME 233, 30 (1965).

[10] S. L. Sass and B. Borie, J. Appl. Crystallogr. 5, 236 (1972).

[11] W. Lin, H. Spalt, and B. W. Batterman, Phys. Rev. B 13, 5158 (1976).

[12] C. W. Dawson and S. L. Sass, Metall. Trans. 1, 2225 (1970).

[13] K. K. McCabe, M. S. thesis, Cornell University, 1970 (unpublished); K. K. McCabe and S. L. Sass, Philos. Mag. 23, 957 (1971).

[14] S. C. Moss, D. T. Keating, and J. D. Axe, in *Phase Transitions—1973,* edited by L. E. Cross (Pergamon, New York, 1973), p. 179.

[15] J. D. Axe, D. T. Keating, and S. C. Moss, Phys. Rev. Lett. 35, 530 (1975).

[16] A. L. J. Chang, W. Krakow, and S. L. Sass, Acta Metall. 24, 29 (1976).

[17] B. Borie, S. L. Sass, and A. Andreassen, Acta Crystallogr. Sect. A 29, 585 (1973); 29, 594 (1973).

[18] T. S. Kuan and S. L. Sass, Acta Metall. 24, 1053 (1976).

[19] All compositions are given in atomic percent.

[20] B. S. Hickman, J. Inst. Metals 96, 330 (1968).

[21] M. J. Blackburn and J. C. Williams, Trans. Metall. Soc. AIME 242, 2461 (1968).

[22] M. K. Koul and J. F. Breedis, Acta Metall. 18, 579 (1970).

[23] D. de Fontaine, N. E. Paton, and J. C. Williams, Acta Metall.

19, 1153 (1971).

[24] N. E. Paton and J. C. Williams, Scr. Metall. 7, 647 (1973).

[25] V content was determined by atomic absorption spectrophotometry, O_2, by inert gas fusion, other impurities, by spark source mass spectrography. All analyses by Northern Analytical Laboratory, 3 Northern Blvd., Amherst, NH 03031.

[26] C. B. Walker, J. Appl. Crystallogr. 15, 352 (1982).

[27] An averge atom calculation, using x-ray scattering factors from D. T. Cromer and J. B. Mann, Los Alamos Scientific Laboratory Report No. LA-3816 (unpublished) and anomalous scattering terms from D. T. Cromer and D. Liberman, J. Chem. Phys. 53, 1891 (1970).

[28] C. B. Walker and D. R. Chipman, Acta Crystallogr. Sect. A 26, 447 (1970).

[29] C. B. Walker, Acta Crystallogr. Sect. A 33, 342 (1977).

[30] Similar relative intensities for coherent versus incoherent particles are also obtained for more complex multisite models discussed in a later section.

[31] B. Borie, Acta Crystallogr. Sect. A 38, 438 (1982).

[32] B. Borie, Acta Crystallogr. Sect. A 30, 337 (1974).

[33] C. B. Walker, J. Phys. Chem. Solids 44, 167 (1983).

[34] J. M. Cowley, Acta Crystallogr. Sect. A 28, S167 (1972).

[35] J. M. Sanchez and D. de Fontaine, J. Appl. Crystallogr. 10, 220 (1977).

[36] Models with a stronger dependence on c_j gave poorer fits.

[37] D. de Fontaine, Acta Metall. 18, 275 (1970).